

Single charge regime electrodynamic force measuring in solution by upconversion photonic force microscope

Xuchen Shan

Beihang University

Lei Ding

University of Technology Sydney <https://orcid.org/0000-0002-9574-5165>

Shihui Wen

University of Technology Sydney <https://orcid.org/0000-0002-4670-4658>

Chaohao Chen

University of Technology Sydney <https://orcid.org/0000-0003-4620-7771>

Dajing Wang

Beihang University

Hongyan Zhu

Beihang University

Peng Nie

Sun Yat-sen University

Xunyu Lu

University of New South Wales

Shen Wang

University of Melbourne

Xiaolan Zhong

Beihang University

Qian Su

University of Technology Sydney

Baolei Liu

Beihang University

Jie Lu

University of Technology Sydney

Peter Reece

University of New South Wales <https://orcid.org/0000-0003-4852-3735>

Lingqian Chang

Beihang University

Dayong Jin

University of Technology Sydney <https://orcid.org/0000-0003-1046-2666>

Fan Wang (✉ fanwang@buaa.edu.cn)

Beihang University <https://orcid.org/0000-0001-7403-3305>

Article

Keywords: Photonic force microscope, upconversion nanoparticle, Attonewton force, Brownian motion

Posted Date: October 14th, 2022

DOI: <https://doi.org/10.21203/rs.3.rs-2160647/v1>

License: © ⓘ This work is licensed under a Creative Commons Attribution 4.0 International License.

[Read Full License](#)

Single charge regime electrodynamic force measuring in solution by upconversion photonic force microscope

Xuchen Shan^{1†}, Lei Ding^{2,3,4†}, Shihui Wen⁵, Chao hao Chen², Dajing Wang¹, Hongyan Zhu¹, Peng Nie⁶, Xunyu Lu⁷, Shen S.J. Wang⁸, Xiaolan Zhong^{1*}, Qian Peter Su³, Baolei Liu¹, Jie Lu⁹, Peter Reece¹⁰, Lingqian Chang¹¹, Dayong Jin^{5,12}, and Fan Wang^{1,2*}

¹School of Physics, Beihang University, Beijing, China.

²School of Electrical and Data Engineering, Faculty of Engineering and Information Technology, University of Technology Sydney, Sydney, NSW, Australia.

³School of Biomedical Engineering, Faculty of Engineering and Information Technology, University of Technology Sydney, Sydney, NSW, Australia.

⁴School of Mathematical and Physical Sciences, Faculty of Science, University of Technology Sydney, NSW 2007, Australia.

⁵Institute for Biomedical Materials and Devices (IBMD), School of Mathematical and Physical Sciences, Faculty of Science, University of Technology Sydney, NSW 2007, Australia.

⁶State Key Laboratory of Biocontrol, School of Life Sciences, Sun Yat-sen University, Guangzhou, China.

⁷Particles and Catalysis Research Laboratory, School of Chemical Engineering, The University of New South Wales, Sydney, NSW 2052, Australia.

⁸Computing and Information Systems Department, Melbourne School of Engineering, University of Melbourne, Melbourne, Victoria, Australia.

⁹Centre for Artificial Intelligence, Faculty of Engineering and IT, University of Technology Sydney, Sydney, New South Wales 2007, Australia.

¹⁰School of Physics, The University of New South Wales, Sydney, New South Wales, Australia.

¹¹Beijing Advanced Innovation Center for Biomedical Engineering, School of Biological Science and Medical Engineering, Beihang University, Beijing 100191, China

¹²UTS-SUSTech Joint Research Centre for Biomedical Materials & Devices, Department of Biomedical Engineering, Southern University of Science and Technology, Shenzhen, People's Republic of China.

†These authors contributed equally.

*Correspondence to fanwang@buaa.edu.cn, zhongxl@buaa.edu.cn

Key Words: Photonic force microscope, upconversion nanoparticle, Attonewton force, Brownian motion

Precise force measurement is critical to probing biological events and physics processes, spanning from molecular motor's motion to the Casimir effect¹ and the detection of gravitational wave². Yet, despite

extensive technology developments, the 3D nanoscale measurement of weak forces in aqueous solutions poses a significant challenge. Techniques that rely on the optically trapped nanoprobe are beset with difficulties, including low light scattering for force measuring and high localization error from their Brownian motion. Here, we report the measurement of the long-distance electrodynamic force on single nanocrystals suspended in aqueous solution with only 11 net charges. To achieve this, we develop an upconversion photonic force microscope that encompasses a diffraction-limited tracking-based force sensing theory and the advance of lanthanide ion resonance force probe^{3,4}. The tracking method is based on neural network empowered super-resolution localization, where the position of force probe is extracted from the optical astigmatism modified point spread function (PSF), enabling the measurement of trap stiffness for nanoparticles through equipartition theorem with a force sensitivity down to 592.9 attoNewtons (aN), that is, 5 times lower than the reported best sensitivity value⁵. We further demonstrate that the technology can measure a single nanocrystal's electrophoresis force and zeta potential, experimentally verifying Loeb's empirical relationship. This work offers new opportunities for detecting single-charge dynamics over long-distance and sub-cellular single molecular level biomechanical force.

Weak force measuring in physiological solutions with high spatial resolution is the ultimate goal of biomechanics in investigating biological events. Tens of nano-Newton force have been used to quantify the magnitude of contractile forces generated by tissue and cells^{6,7}. Tens of pico-Newton force measuring are applied to study the traction forces imparted by contractile during the single cell migration⁸⁻¹⁰. Sub-pico-Newton force is associated with a string tension of a single DNA molecule and the organization of chromosomes¹¹. Cantilever-based force microscopy¹²⁻¹⁵ and microtube force spectroscopy¹⁶⁻¹⁹ are popular tools yet have limited spatial mapping dynamics; molecular force microscopy is powerful while having a limited dynamic force range²⁰⁻²²; optical tweezers are often used as a dynamic tool to trap a force probe for measuring and generating nano-Newton to femto-Newton force in three-dimensional (3D), namely a photonic force microscope²³ (PFM, Fig. 1a). The fundamental limitation of the PFM is the reduced scattering signal of the force probe with the decrease of its size. As a result, simultaneously achieving high spatial resolution and high force sensitivity remains a challenge.

Trapping in vacuum^{24,25} and active feedback cooling^{2,26} are efficient ways to circumvent Brownian motion, achieving zepto-Newton²⁴ force sensing by tracing the variation of the motion power spectrum. While obviously, these methods cannot be used for bio-force sensing since living cells cannot survive in a vacuum. In physiological solution, another limitation of force sensing is the feeble scattering intensity of nanoparticles since most of methods are to sense the signal change in scattering^{23,27-32}, and the Rayleigh scattering cross-section is related to a nanoparticle's size by the power of six. Based on materials with higher refractive indices^{33,34} or noise reduction, the smallest force sensitivity can only go down to 2.4 - 8 femto-Newton^{5,35} by PFM, yet far from the sub-femto-Newton that is required for emerging fields of far-field charge interaction³⁶. Beyond that, the heat generated by trapping metallic particles will hinder PFM's bio-application³⁷.

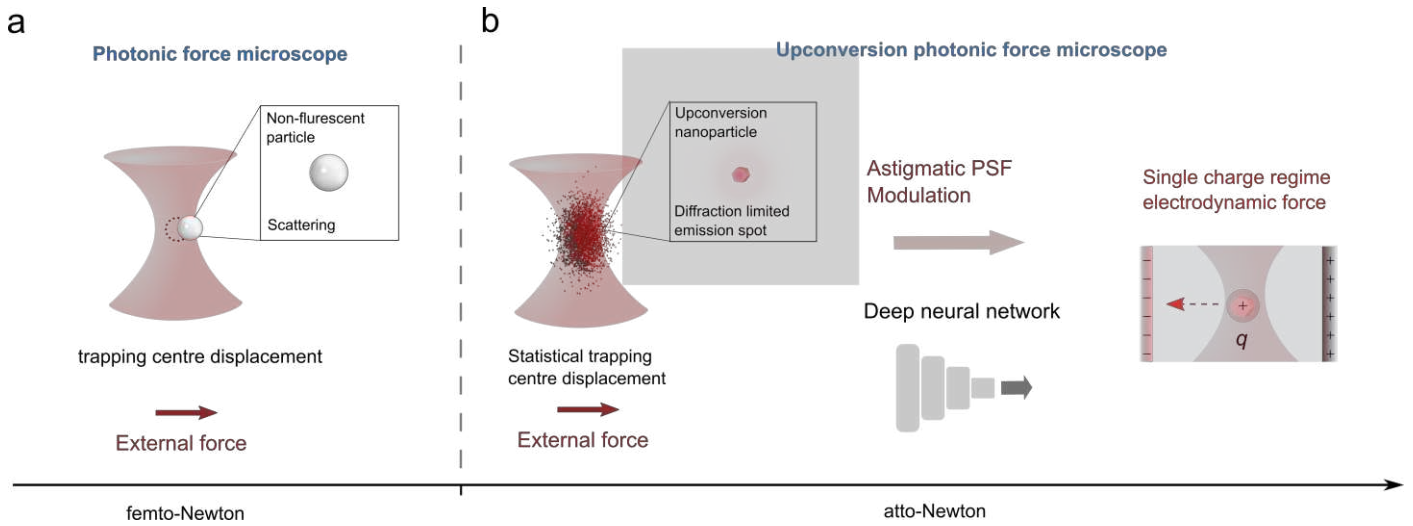


Figure 1. Diagram of the upconversion photonic force microscope. **a**, Diagram of a traditional photonic force microscope that relies on the detection of the scattering signal from the large particle with force sensitivity down to the femto-Newton range. **b**, The upconversion photonic force microscope utilizes the upconversion nanoparticle as the force probe and detects its statistical trapping centre displacement from the diffraction-limited emission spot. With the advances in astigmatic PSF modulation and deep neural network, the force sensitivity has been enhanced to sub-femto-Newton, achieving a single charge regime.

Video tracking microscopy³⁸ allows the calculation of trap stiffness from the trajectory of optically trapped particles, circumventing the measurement of the weak scattered field. Adopting fluorescence video tracking, we developed a force sensing technology herein based on precisely measuring the statistical centre of the position distribution of an optically trapped nanoparticle. Compared with tracking the trapping centre displacement (Fig. 1a) used for nano-Newton force sensing such as cell deformation, detecting the variation on the statistical centre of the diffraction-limited point spread function of the trapped nanoparticle has the opportunity to achieve atto-Newton force sensing with nanometre spatial resolution (Fig. 1b). The key is to achieve the super-resolved 3D tracking localisation which is a challenge for optically trapped nanoparticle due to the Brownian motion induced localisation error. Inspired by 3D single molecular localisation microscopy³⁹, we build astigmatism optical tweezers with deep neural network-empowered calibration for super-resolved localisation. The resultant force sensing method encompasses the benefits of high spatial resolution and force sensitivity with potential advantages in sensing long-distance electrodynamic interaction.

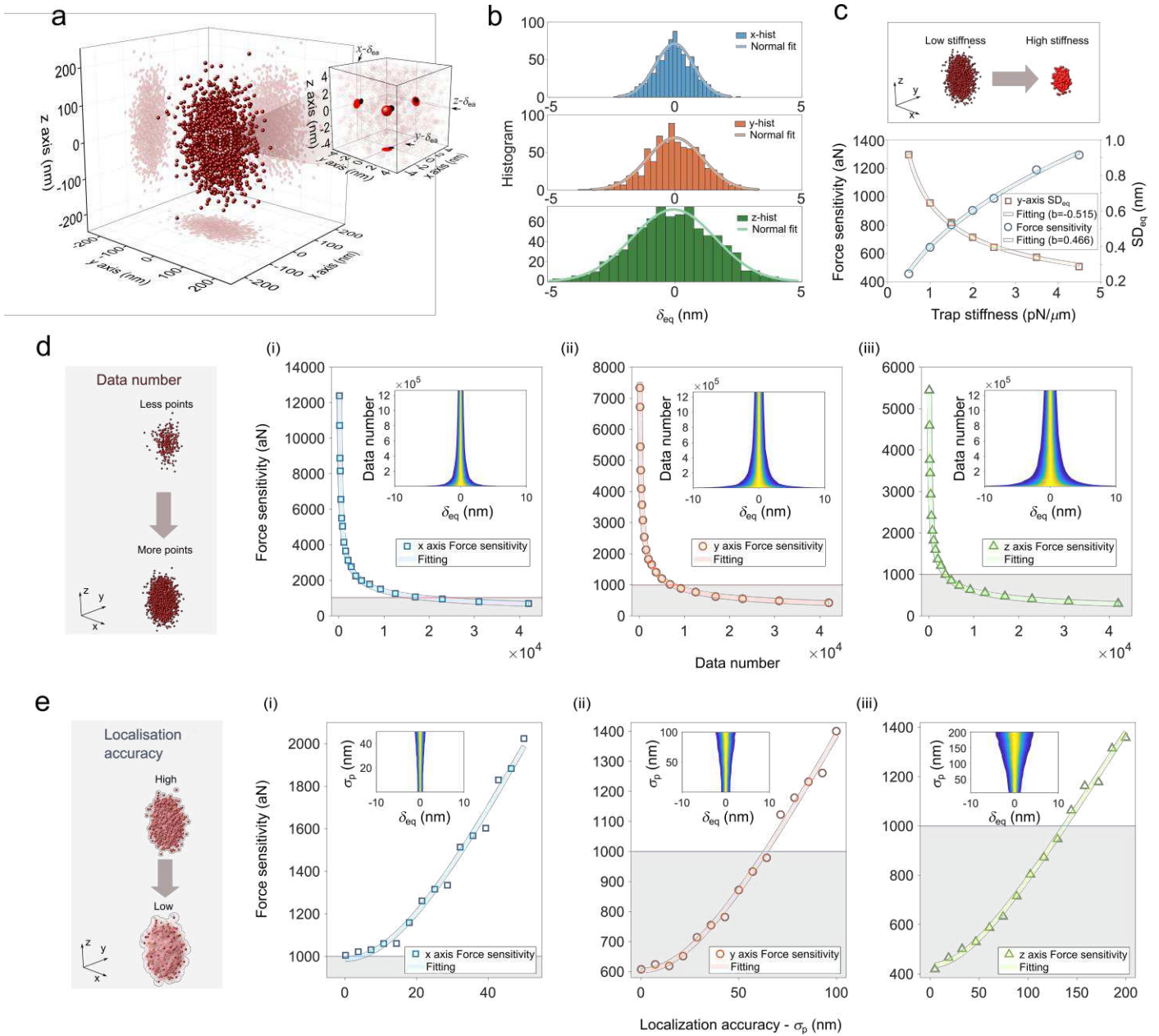


Figure 2. Monte Carlo trapping simulation to analyse the force sensitivity. **a**, 3D positions and the projections of a single trapped nanoparticle. The black and red dots in the inset indicate the origin of coordinates and the distribution centre, respectively. The shift of the central location (δ_{eq}) for x-, y- and z-axis are 0.7429, 1.0859, and 1.6386 nm, respectively. **b**, The statistic histogram of δ_{eq} by repeating the measurement in **(a)** for 800 times. **c**, The role of trap stiffness (y-axis) on force sensitivity. Upper, the schematic of the trapped nanoparticle's position distribution with low and high trap stiffness. Bottom, the simulated force sensitivity and position shift accuracy vary with trap stiffness. Here σ_p is 0. **d**, The role of data number on force sensitivity. Left, the schematic of the trapped nanoparticle's position distribution with different data numbers. Right, force sensitivity varies with the data number for x- (i), y- (ii) and z-axis (iii). Here σ_p is 0. **e**, The role of localization accuracy on force sensitivity. Left, the schematic of the trapped nanoparticle's position distribution with high and low localisation accuracies. Right, the force sensitivity varies with localization accuracy for x- (i), y- (ii) and z-axis (iii). The nanoparticle radius used here is 23.3 nm. The laser power for **a**, **b**, **d**, and **e** is 35.8 mW and for **c** is from 10 to 90 mW. The data number is 1,610. **(a)**, 10,000 **(c)** and 20,000 **(e)**. The trap stiffnesses for 35.8 mW are 0.137, 0.05, and 0.026 pN/ μ m/mW for x-, y- and z-axis, respectively. The insets in **d** (i-iii) and **e** (i-iii) are the statistic histogram of δ_{eq} for different data numbers and localization, respectively.

We first simulate the force sensitivity and employ lanthanoid ions doped nanoparticles (Ln-NPs), also called upconversion nanoparticles, as the force probe since these particles have strong trap stiffness³ and high emission intensity while less heat generation^{40,41}. According to the equipartition theorem⁴², the position of an optically trapped nanoparticle has a 3D Gaussian distribution. Any constant external force will push the distribution centre's location to generate restoring force and balance this external driving force. Therefore, the external force can be directly measured by detecting the shift of the central location (δ_{eq}) away from its original equilibrium position, with $F_{ex} = k\delta_{eq}$, where k is the trap stiffness. The force sensitivity is $\Delta F_{ex} = kSD_{eq}$, where SD_{eq} is the standard deviation of the detected distribution shifts (δ_{eq}). Fig. 2a shows simulated position distribution of the optically trapped nanoparticle with trapping centre at the origin (black dots in the inset), while the averaged position centre (red dots in the inset) shows offsets from the origin. Note that the offsets come from the random distribution by Brownian motion rather than from the external force. Repeating the measurement of δ_{eq} for 800 times, the histogram of offsets (Fig. 2b) indicates a Gaussian distribution with standard deviation SD_{eq} . Similar to the localisation accuracy for single molecule localization microscopy⁴³, the SD_{eq} is calculated by considering the errors introduced by distribution probability and the uncertainty of the statistic points. Here the probability of one nanoparticle shown at the detected position is a convolution of the trapping potential well induced position distribution and the emitter's detecting location distribution (see Supplementary Information S2 for detail). The formular of force sensitivity is derived as:

$$\Delta F_{ex} = kSD_{eq} = \sqrt{\frac{(k\sigma_p)^2 + (k_B T)k}{N - \frac{3}{N_h^2}}} \quad (1)$$

where k is the trap stiffness, σ_p is the imaging localisation accuracy, k_B is the Boltzmann's constant, T is the experimental temperature, N is the total scatters' number and N_h is the binning number for histogram.

We use Monte Carlo trapping simulation to verify the developed formula and investigate the best sensitivity. According to equation (1), the force sensitivity can be optimized by tuning the parameters. To obtain the impact of trap stiffness on sensitivity, we assume the imaging localisation is absolutely accurate ($\sigma_p=0$). The measured SD_{eq} shows the power of -1/2 relation with trap stiffness, as shown in Fig. 2c orange square, matching with prediction. The minimum sensible force increases with trap stiffness with a power of 1/2 (labelled by blue circles), which indicates that the smallest trapping stiffness should be used to obtain the highest sensitivity. To this end, the axial force sensing will have better sensitivity due to smaller stiffness. Experimentally, the minimal trap stiffness for stable and long-time trapping of a single 50 nm UCNP is 4.9, 1.79, and 0.93 pN/ μm for x, y, and z-axis, respectively. Fig. 2d shows that a larger data number narrows down the histogram (inset), with SD_{eq} hyperbolically decreases. Here we take the minimal experimental localisation error $\sigma_p=0$ to show the highest achievable sensitivity. In this condition, the simulated sensitivity values for x, y, and z-axis (Fig. 2d i-iii) decrease with data number with a power of -1/2, consistent with the simplified equation $\Delta F_{ex} = \sqrt{k_B T k / N}$. This result suggests that minimum data numbers 20000, 7000, and 3800 are

required to achieve a force sensitivity below 1fN for x , y , and z axes, respectively. Fixing the trap stiffness as the minimum experimental value, and the data number as 20000, the optimized sensitivities are obtained by considering the minimal experimental σ_p , according to equation 1. Smaller σ_p (higher localization accuracy) offers smaller SD_{eq} (Fig. 2e, inset) and better force sensitivities (Fig. 2e i-iii). To maintain the sensitivity below 1000 aN, the localization accuracy has to be higher than 4, 64, and 137 nm for the x , y and z axes, respectively.

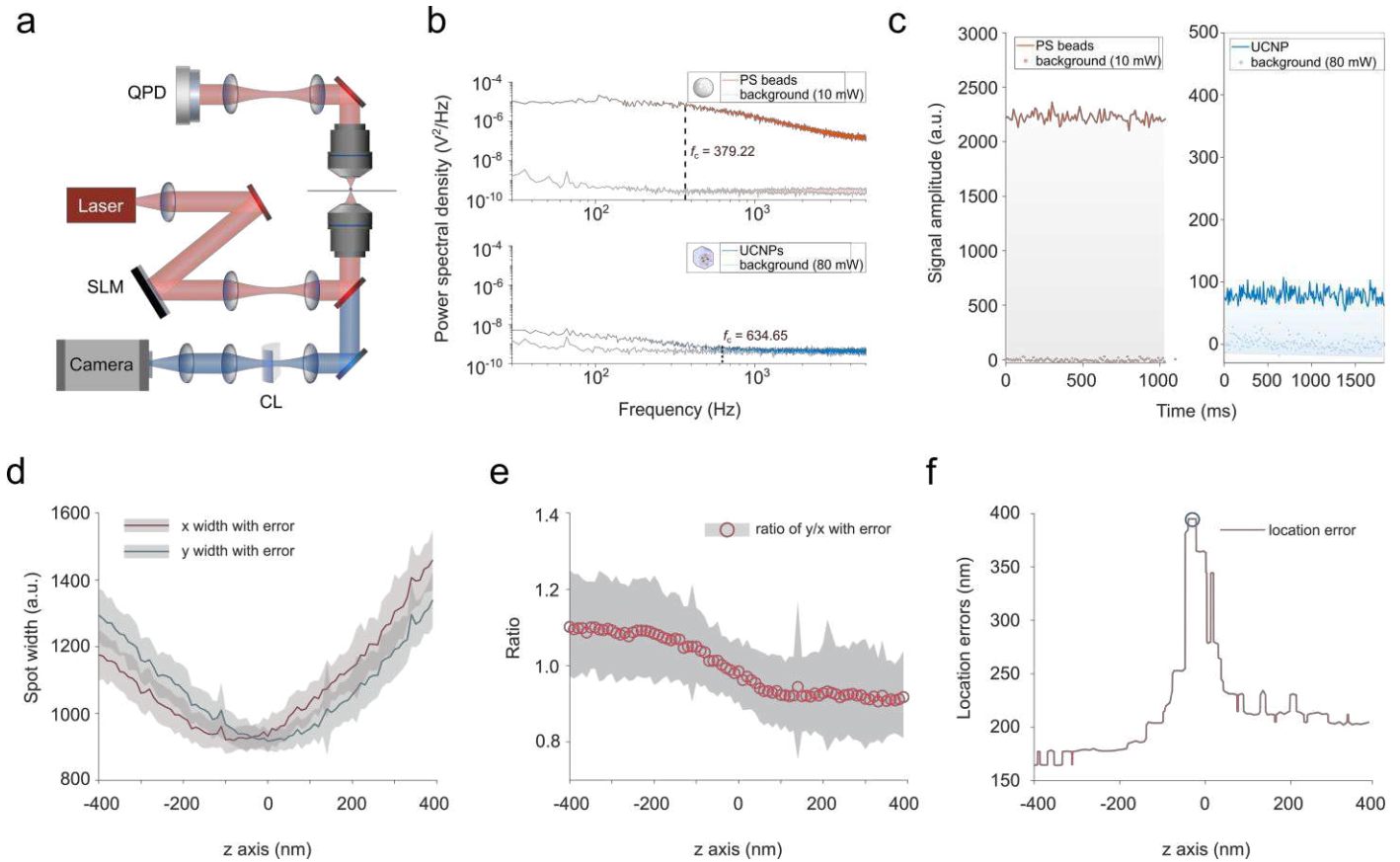


Figure 3. Axial localisation estimation by fluorescence-based astigmatism-enhanced optical tweezers. **a**, schematic of astigmatism-enhanced optical tweezers. A cylindrical lens (CL) is introduced for optical astigmatism (see Supplementary Information S6). QPD, quadrant photodiode detector, SLM, spatial light modulator. **b**, Experimentally measured power spectrums for optically trapped 1 μ m polystyrene sphere (PS) bead (FluoSpheresTM carboxylate red fluorescent (580/605), ThermoFisher Scientific) and lanthanide-doped nanoparticle (NaYF₄:20%Yb,2%Er, diameter, 58 nm). The power of 976.5 nm laser is 10 mW for the PS bead (two-photon absorption excitation) and 80mW for the Ln-NP, respectively. Data acquisition rate is 1,000,000 Hz for both PS bead and Ln-NP. The trap stiffness of the PS bead calculated by fitting the spectra is 2 pN/ μ m/mW for y-axis and consequently the frequency corner f_c is 379.22 Hz. The trap stiffness of the Ln-NP is calculated by the video tracking method as 0.0485 pN/ μ m/mW, and the calculated frequency corner f_c is 634.65 Hz (see Supplementary Information S4 for the details). **c**, Video intensity tracking of optically trapped particles. For 1 μ m PS bead, the laser power is 10 mW, and the exposure time is 0.1 s. For Ln-NP, the laser power is 80 mW and the exposure time is 0.001s. **d**, Lateral variations of the PSF width at different z positions. 976.5-nm laser power is 96 mW, and the exposure time is 0.01s. $z=0$ stands for the axial trapping centre. **e**, The y-x ratio of PSF width varies with the axial position (z), which is the calibration curve for finding the axial position of a trapped emitter. The error arises from the Brownian motion of the trapped particles. **f**, Location errors of an optically trapped

emitter at different axial positions, according to the calibration curve (e). Note that using the PSF of particles on glass slide with aberration correction to create the calibration curve would decrease the localisation error (see Supplementary Fig. 6) yet not achieving the required resolution.

We further developed astigmatism optical tweezers to achieve the desired nanoscale localization accuracy for sub-femto-Newton force sensing. Figure 3a shows the optical system, where a QPD (quadrant photodiode detector) is used to detect the scattering field, and the camera captures the focus images for extracting the 3D location. Tracking voltage change in QPD⁴² can exact the 3D position, but the weak scattering and the Brownian motion of nanoparticles lead to considerable errors in the localisation. Large particles such as 1 μ m polystyrene sphere bead with a high scattering cross-section could have a good signal-to-background ratio as shown on the power spectrum (Fig. 3b, upper). While nanoparticles (e.g. Ln-NPs) have much weaker scattering strength. As a result, the high-frequency region (including the corner frequency range) of its power spectrum curve is undistinguished from the background (Fig. 3b, bottom); hence the corner frequency and trap stiffness of trapped Ln-NPs cannot be obtained by fitting the curve. As a contrast, both dye-stained sphere and nanoparticle have an eminent signal-to-background ratio during multiphoton fluorescence image (Fig. 3c). Indeed, video tracking of nanoscale fluorophores generally have a great signal-to-background ratio that is optimised by super-resolution microscopies. The large anti-Stokes excitation of Ln-NPs can further suppress the background.

A sCMOS camera captures the fluorescence image, and we place a cylinder lens (CL) into the imaging path to introduce optical astigmatism, thereby encoding the axial position information into the 2D image. The cylinder lens adds a parabolic phase in the horizontal direction of the image that shifts the horizontal focus and modifies emitters' point spread function (PSF) to an "elliptical" shape when the emitters are out of focus (Supplementary Information, S6 and Fig. 6). Typically, the pre-characterized PSF waist sizes (both x and y) are used to deduce emitters' axial position^{39,44-46}. However, due to the Brownian motion, this typical characterisation method is not working efficiently for optical tweezers. The optically trapped particle can be treated as inside a 3D harmonic potential well, leading to a Gaussian distribution of the position on each axis. The spatial light modulator (SLM) controls the central position of the distribution but not the individual transient positions. This, in turn, results in a large error on the PSF waist (Fig. 3d) and the waist ratio (Fig. 3e) from the axial position variations. In extreme cases, when the waist ratio is 0.99, the localisation error is as large as 395 nm. Fig. 3f is the localisation error for different distances, which cannot afford an aN sensitivity.

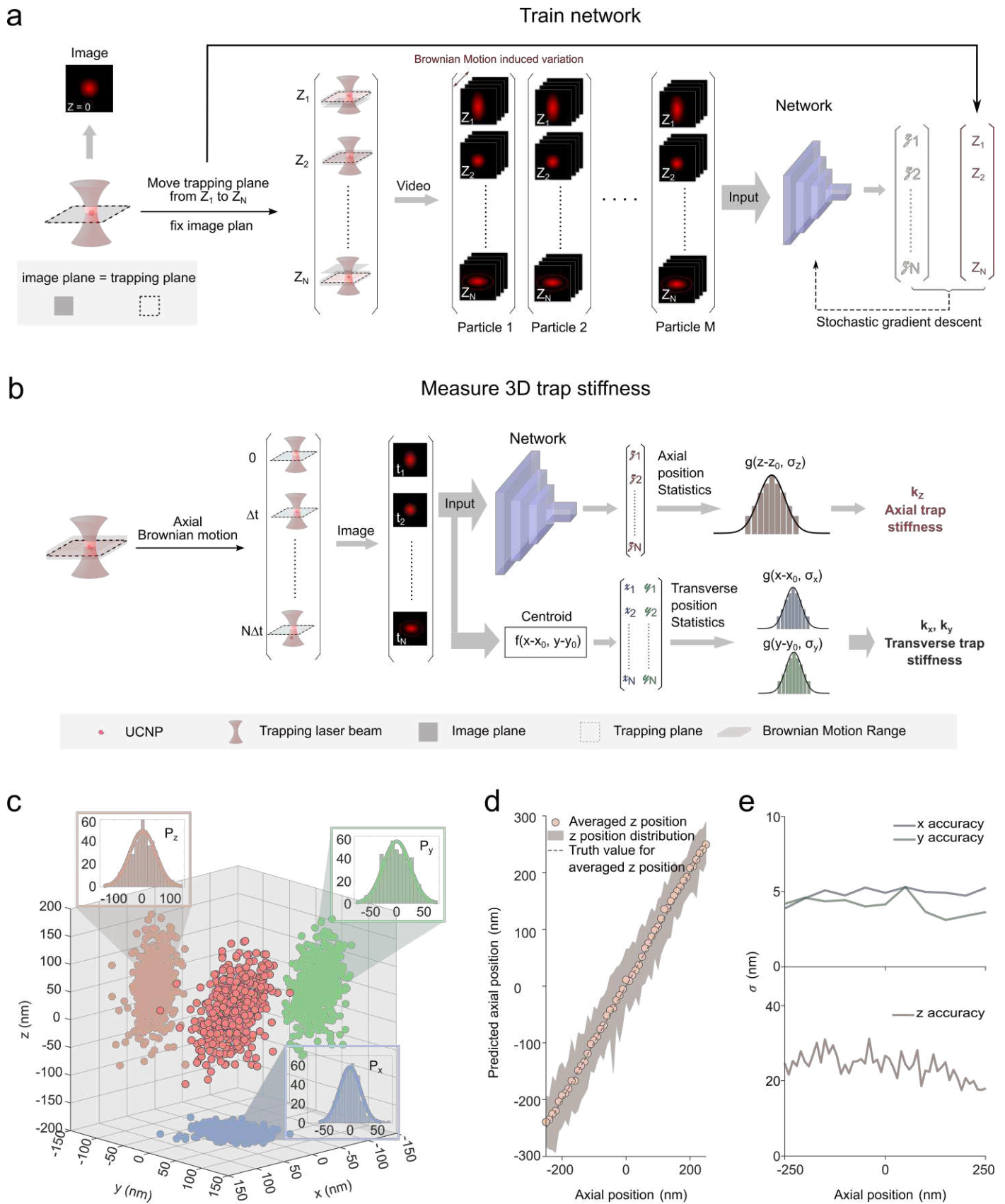


Figure 4. Deep neural network-empowered optical astigmatism video tracking method. **a**, Construction of a machine learning model, where the astigmatic PSF features are recognized and classified via recording the videos of the trapped nanoparticles at different z positions. The SLM controls z position (Z_1 to Z_N) (see Supplementary Information for more details, S7). **b**, 3D trapping stiffness measurement of single nanoparticles at an unknown z position. Axial trapping stiffness is obtained by machine learning, and lateral stiffness is achieved by a centroid method (see Supplementary Information for more details, S7). **c**, Measured 3D position distribution of an optically trapped Ln-NP

under 96 mW of a 976.5-nm laser. Insets are the histogram of the position on x , y , and z -axis. **d**, Axial positions of the trapped single nanoparticles obtained by our machine learning algorithm. The pink circles denote the averaged axial position value using our algorithm, the dashed line is the truth value of the set averaged axial position, and the bisque area represents the distribution of the transient position of the trapped single nanoparticles. The truth value is controlled by the SLM. **e**, 3D positions accuracies by our deep neural network model.

Here we build a deep neural network⁴⁷ to improve the localisation accuracy of the astigmatism optical tweezers. In the training stage (Fig. 4a), a single nanoparticle is initially trapped at the $z=0$ position (arbitrary trapping position above the coverslip). Modulated by SLM, the trapping centre/laser centre is actively moving to the axial positions from Z_1 to Z_N , while the imaging plane is fixed on $z=0$. Due to the Brownian motion, the trapped nanoparticle is moving around the trapping centre within a range. The network would learn the spatial features from the group of images. Note that the position label refers to the central position of the distribution rather than the individual positions for each image. The weight of each image is regulated by the repeatability of characteristic (increase weight) on a single central position and the overlapping of characteristic (increase weight) between different positions. As a result, the regulated weights would train the network to predict the central position of a single 2D frame. In the applying stage (Fig. 4b), a single nanoparticle is trapped at $z=0$ position, while its instant position varies within a small range with time. Taking a video of the emission patterns for 100s will generate a series of images (e.g., 10000 slides), and the trained DNN can convert each image into axial position values. The lateral trap stiffnesses are extracted from these images through the centroid finding method⁴⁸. The statistic of positions can be fitted into $P(x) \propto \exp\left(-\frac{k(x)^2}{2k_B T}\right)$ (see Supplementary Information for more details, S2), to extract the 3D trap stiffness. Figure 2c shows the 3D position tracking of an optically trapped Ln-NP (500 frames), applying our trained DNN. Under the trapping power of 35.8 mW, the calculated trap stiffness are 0.137, 0.05, 0.026 pN/ $\mu\text{m}/\text{mW}$ for x , y , and z direction respectively, which matches with the theoretically calculated values³. The position distribution is strongly confined in x direction since the beam waist is smaller in x direction, while the beam is linearly polarized in y direction. The weak trap stiffness in z direction leads to a large axial position distribution. Here we further use the statistic centre of the axial position distribution to verify the axial localisation accuracy (Fig. 4d). The truth statistic centre value is controlled by the SLM (dashed line), and the measured statistic centre (pink circle) is estimated from the measured axial positions of different frames for each of axial positions. Benefiting from DNN and astigmatism modulation, the root-mean-square errors (RMSE) in z direction between the truth value and the measured value are below 30nm (Fig. 4e, bottom). The RMSE in x and y direction are obtained by comparing the positions with the total averaged values, with the accuracy of about 5 nm (Fig. 4e, upper). Combining the advantages of ion resonance upconversion nanoparticles, optical astigmatism based super-resolved localisation, and deep neural network empowered optical tweezers, we define the technology as upconversion photonic force microscope (UPFM).

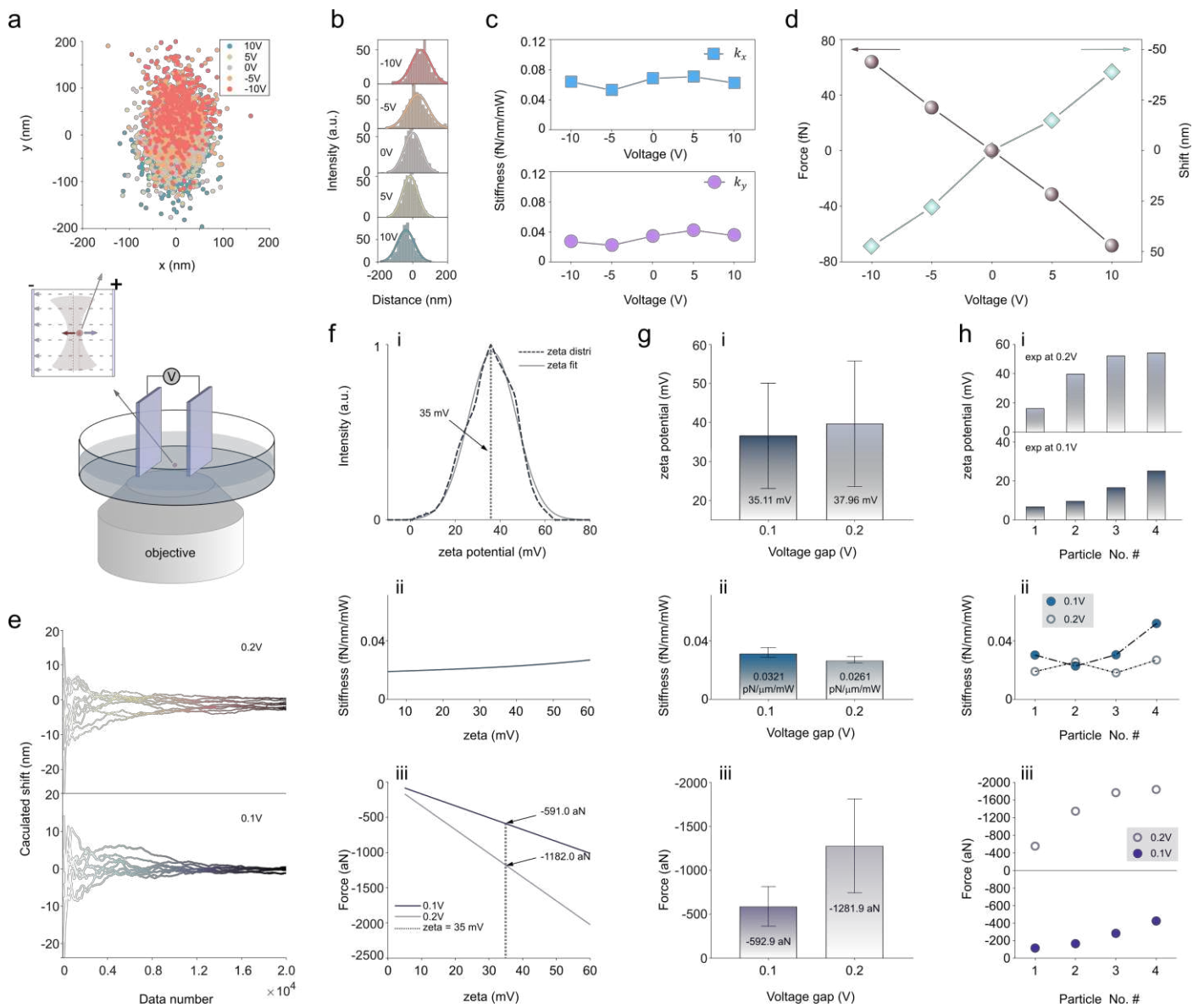


Figure 5. Measuring the electrodynamic force of a single trapped nanoparticle by UPFM. **a-d**, Investigation of the trapped single nanoparticles under large applying electric potentials. **a**, Bottom, schematic setup of measuring electrodynamic forces for the trapped single nanoparticles within the uniform electric field. The distance between two electrodes is 1 cm. The potential applied between the electrodes is controlled in the range of -10 to 10 voltage (V) by a homemade Labview program. Upper, the scatter plots of the trapped single nanoparticle under different applying potentials. **b**, Position distribution of the trapped single nanoparticle on y-axis (low optical force direction) under different applying potentials. **c**, The corresponding transverse trap stiffness calculated under different applying potentials. **d**, Position shift and resultant force under different applying potentials. **e**, The effect of data number on the calculated position shift. The lines with different colours represent different trapped nanoparticles under 0.1 V and 0.2 V electric potentials, respectively. **f-h**, Investigation of the trapped single nanoparticles under small applying potentials. **f**, Measured zeta potential (i) of bulk solution of nanoparticles by the Zetasizer, the accordingly calculated trap stiffness (ii) and force (iii) under 0.1 V and 0.2 V, respectively. **g**, The statistics value of zeta potential (i), trap stiffness (ii), and force (iii) from the measured single trapped nanoparticles (at least 8 nanoparticles). The results represent the mean \pm s.e.m. of $n = 8$ trapped single nanoparticles for 0.1 V, and $n = 9$ for 0.2 V. **h**, The individual value of zeta potential (i), trap stiffness (ii), and force (iii) from the single trapped nanoparticles. The used power of 976.5 nm laser is 50mW. Data number is 500 for a-d and 20,000 for f-h.

According to Fig 2e-ii, 5 nm localisation in the y direction will induce a force sensitivity of 600 aN. We use the electrodynamic force on single nanoparticles to verify the force sensitivity experimentally. The surface double charged layer around nanoparticles, which induces zeta potential, can be converted into the surface net charge⁴⁹, in terms of analysing the electrodynamic force. Hence, placing electrodes around the nanoparticle (Fig. 5a, bottom) and adding electric potentials would generate external force on particles and continuously shift its statistic trapping centre (Fig. 5b). Though the centre is shifting, the transverse trap stiffness would keep the similar values (Fig. 5c). Figure 5d shows the centre shifting values under different potentials (labelled light green), which is used to calculate the electrodynamic force (labelled brown). Taking the trap stiffness variation (Fig. 5c) under different potentials into account, the measured electrodynamic force shows a straight line from 64 fN to -68 fN (the negative sign represents the force direction according to the electric field). Verifying the capacity to detect hundreds of aN forces requires small electric potentials such as 0.2 V and 0.1 V, with high data accusation numbers.

Figure 5e experimentally verifies how the data number affects the force sensing result. We have selected individual nanoparticles to track their centre shifts with different data numbers under external potentials of 0.2 V and 0.1 V, respectively. The shift value is gradually achieving the plateau with more data numbers. The number 20,000 provides a stable central shift value for 600 aN force sensitivity (Fig. 2d). The synthesized Ln-NPs have a zeta potential distribution from 15 to 60 mV with a mean of 35 mV (Fig. 5f-i, measured by a Zetasizer). The simulation shows that increasing zeta potential will increase the trap stiffness (Figure 5f-ii), but the trap stiffness would be in the range of 0.019 to 0.027 pN/ $\mu\text{m}/\text{mW}$. The electrodynamic forces on particles with different zeta potential (Fig. 5f-iii) are calculated based on its Lorentz forces and Loeb's empirical relationship^{50,51} (equation 2, also see Supplementary material S8 for details).

$$\sigma(\phi) = \varepsilon_0 \varepsilon \kappa \frac{k_B T}{ze} \left\{ 2 \sinh\left(\frac{z\phi}{2}\right) + \frac{4}{\kappa a} \tanh\left(\frac{z\phi}{4}\right) \right\} \quad (2)$$

where ε_0 is vacuum permittivity, ε is relative permittivity (dimensionless) of the aqueous solution, k_B is Boltzmann constant, z is the valence of ion, e is the electron charge, $\phi = e\varphi/k_B T$ is the reduced (dimensionless) zeta potential. κ^{-1} is the length of the Debye Shield given by $\kappa^2 = \frac{e^2 n N_A \cdot 10^3}{k_B T \varepsilon_0 D}$, where n is the total concentration of ions (positive and negative), N_A is Avogadro constant.

Experimentally, our force sensing technology also works as an in-suit zeta potential measuring method, applying Loeb's empirical relationship. We measured 8 and 9 particles with electric potential of 0.1 V and 0.2 V, respectively, the mean value of zeta potential is 35.11 mV and 37.96 mV (Fig. 5g-i), respectively, matching the characterized value. The averaged value of the measured trap stiffnesses are 0.0321 and 0.0261 pN/ $\mu\text{m}/\text{mW}$ within the predicted range. Figure 5g-iii indicates the force sensitivity verifying the result. The mean of the measured electrodynamic forces is 592.9 aN and 1,281.9 aN for 0.1 V and 0.2 V, respectively, and the error bar is mainly from the sample variation on the zeta potentials. These measured forces match with the predicted value (Fig. 5f-iii), and the force difference of 689 aN induced by 0.2 V and 0.1 V could be clearly

recognized. The consistency between zeta potential, trap stiffness and electrodynamic force indicates that our method's accuracy and force sensitivity is down to at least 592.9 aN. It also verifies the Loeb's empirical relationship is valid for the nanoscale regime.

We further use the method to detect the force of individual particles. Our force estimation method shows the measured individual zeta potentials range from 6.8 to 54.5 mV (Fig. 5h-i). The trap stiffnesses (Fig. 5h-ii) are generally within the predicted range, and the higher stiffness for #4 (0.1 V) may result from a slightly larger size. Fig. 5h-iii shows the detected electrodynamic force on each nanoparticle, where an extreme case (a particle with a small zeta potential value) of 114.2 aN could be detected though the measuring accuracy is around 600 aN. Note that the measurement works for all voltage values, and higher voltages produce larger forces for the same zeta potential value. With 2V, an electrodynamic force of 363 aN is detected, which indicates the particle has a surface net charge of only 11 charges (see Supplementary material S9). Further increasing electric potential or decreasing the distance between the electrodes would push the detecting limit down to a single charge.

In conclusion, we have demonstrated that UPFM, a reliably nanoscale 3D sub-fN force sensing technology in a physiological solution, can be realized by adding a single astigmatism element to conventional optical tweezers. By applying a deep neural network to extract the 3D position with nanometer resolution from 2D fluorescence video tracking a diffraction limit spot, the position distribution of the trapped nanoparticle and the statistical centre shifting can be detected. The high accuracy of the localization with the high signal-to-background ratio enables a force sensitivity as high as 600 aN which is 5 times more sensitive than the best-reported value. We demonstrate that our technology can detect the electrodynamic force and the zeta potential of a single nanoparticle with only 11 net charges, reducing the distance between electrodes would improve the sensitivity to a single net charge (see Supplementary material S9). The strategy that leverages diffraction-limited tracking of nanoparticles is predicted to be compatible with other types of fluorescent nanoparticles and other imaging modality. The sensitivity could be further improved by further engineering the PSF⁵² of nanoparticles to increase the localisation accuracy. In part on the strength of video tracking, our method has strong potential for large field multiple spots simultaneously force sensing by applying multiple trappings, which also saves the force mapping time. The method could also work as one type of optical tweezers-based scanning probe microscopy⁵³, and its working mode of detecting the fluorescence signal avoids the scattering-induced localisation error. The aN sensitivity and the advent of Ln-NPs give our technology a promising future in subcellular bio-nanoscience. The functionalized Ln-NPs could be linked to bio-particles such as exosomes and integrins to detect the nanoscale minuscule force interaction. Our method also provides a way for multifunctional perturbation sensing that correlates the temperature sensing⁵⁴, cooling⁵⁵ and heating⁵⁶ capacity of Ln-NPs with the force sensing.

References

1. Chan, H. B., Aksyuk, V. A., Kleiman, R. N., Bishop, D. J. & Capasso, F. Quantum mechanical actuation of microelectromechanical systems by the Casimir force. *Science* (80-.). **291**, 1941–1944 (2001).
2. Arvanitaki, A. & Geraci, A. A. Detecting high-frequency gravitational waves with optically levitated sensors. *Phys. Rev. Lett.* **110**, 1–5 (2013).
3. Shan, X. *et al.* Optical tweezers beyond refractive index mismatch using highly doped upconversion nanoparticles. *Nat. Nanotechnol.* **16**, 531–537 (2021).
4. Ding, L. *et al.* Lanthanide Ion Resonance-Driven Rayleigh Scattering of Nanoparticles for Dual-Modality. *Adv. Sci.* 2203354 (2022).
5. Zensen, C., Villadsen, N., Winterer, F., Keiding, S. R. & Lohmüller, T. Pushing nanoparticles with light - A femtonewton resolved measurement of optical scattering forces. *APL Photonics* **1**, (2016).
6. Ting, L. H. *et al.* Contractile forces in platelet aggregates under microfluidic shear gradients reflect platelet inhibition and bleeding risk. *Nat. Commun.* **10**, 1–10 (2019).
7. Hultin, S. *et al.* Amotl2 links ve-cadherin to contractile actin fibres necessary for aortic lumen expansion. *Nat. Commun.* **5**, (2014).
8. Blakely, B. L. *et al.* A DNA-based molecular probe for optically reporting cellular traction forces. *Nat. Methods* **11**, 1229–1232 (2014).
9. Yamaguchi, N. *et al.* Rear traction forces drive adherent tissue migration in vivo. *Nat. Cell Biol.* **24**, 194–204 (2022).
10. Brockman, J. M. *et al.* Live-cell super-resolved PAINT imaging of piconewton cellular traction forces. *Nat. Methods* **17**, 1018–1024 (2020).
11. Meijering, A. E. C. *et al.* Nonlinear mechanics of human mitotic chromosomes. *Nature* **605**, 545–550 (2022).
12. T. D. Stowe *et al.* Attonewton force detection using ultrathin silicon cantilevers. *Appl. Phys. Express* **71**, 288–290 (1997).
13. Bian, K. *et al.* Scanning probe microscopy. *Nat. Rev. Methods Prim.* **1**, (2021).
14. Alunda, B. O. & Lee, Y. J. Review: Cantilever-based sensors for high speed atomic force microscopy. *Sensors* **20**, 1–39 (2020).
15. Moser, J. *et al.* Ultrasensitive force detection with a nanotube mechanical resonator. *Nat. Nanotechnol.* **8**, 493–496 (2013).
16. Huang, J. *et al.* The kinetics of two-dimensional TCR and pMHC interactions determine T-cell responsiveness. *Nature* **464**, 932–936 (2010).
17. Chen, Y. *et al.* An integrin $\alpha\text{IIb}\beta\text{3}$ intermediate affinity state mediates biomechanical platelet aggregation. *Nat. Mater.* **18**, 760–769 (2019).
18. Ju, L. *et al.* Compression force sensing regulates integrin $\alpha\text{IIb}\beta\text{3}$ adhesive function on diabetic platelets. *Nat. Commun.* **9**, (2018).
19. An, C. *et al.* Ultra-stable Biomembrane Force Probe for Accurately Determining Slow Dissociation Kinetics of PD-1 Blockade Antibodies on Single Living Cells. *Nano Lett.* **20**, 5133–5140 (2020).
20. Stabley, D. R., Jurchenko, C., Marshall, S. S. & Salaita, K. S. Visualizing mechanical tension across membrane receptors with a fluorescent sensor. *Nat. Methods* **9**, 64–67 (2012).
21. Liu, Y., Galior, K., Ma, V. P. Y. & Salaita, K. Molecular Tension Probes for Imaging Forces at the Cell Surface. *Acc. Chem. Res.* **50**, 2915–2924 (2017).
22. Brockman, J. M. *et al.* Mapping the 3D orientation of piconewton integrin traction forces. *Nat. Methods* **15**, 115–118 (2018).
23. Florin, E. L., Pralle, A., Stelzer, E. H. K. & Hörber, J. K. H. Photonic forcemicroscope calibration by thermal noise analysis. *Appl. Phys. A Mater. Sci. Process.* **66**, 75–78 (1998).
24. Ranjit, G., Cunningham, M., Casey, K. & Geraci, A. A. Zeptonewton force sensing with nanospheres in an optical lattice. *Phys. Rev. A* **93**, 1–5 (2016).
25. Ranjit, G., Atherton, D. P., Stutz, J. H., Cunningham, M. & Geraci, A. A. Attonewton force detection using microspheres in a dual-beam optical trap in high vacuum. *Phys. Rev. A - At. Mol. Opt. Phys.* **91**, 1–6 (2015).
26. Gieseler, J. *et al.* Optical tweezers - from calibration to applications: a tutorial. *Adv. Opt. Photonics* **13**, 74 (2021).
27. Bechhoefer, J. & Wilson, S. Faster, cheaper, safer optical tweezers for the undergraduate laboratory. *Am. J. Phys.* **70**, 393–400 (2002).
28. Viana, N. B., Freire, R. T. S. & Mesquita, O. N. Dynamic light scattering from an optically trapped

- microsphere. *Phys. Rev. E - Stat. Physics, Plasmas, Fluids, Relat. Interdiscip. Top.* **65**, 11 (2002).
29. Gibson, G. M., Leach, J., Keen, S., Wright, A. J. & Padgett, M. J. Measuring the accuracy of particle position and force in optical tweezers using high-speed video microscopy. *Opt. Express* **16**, 14561 (2008).
 30. Volpe, G., Volpe, G. & Petrov, D. Brownian motion in a nonhomogeneous force field and photonic force microscope. *Phys. Rev. E - Stat. Nonlinear, Soft Matter Phys.* **76**, 1–10 (2007).
 31. Berg-Sørensen, K. & Flyvbjerg, H. Power spectrum analysis for optical tweezers. *Rev. Sci. Instrum.* **75**, 594–612 (2004).
 32. Pérez García, L., Donlucas Pérez, J., Volpe, G., V. Arzola, A. & Volpe, G. High-performance reconstruction of microscopic force fields from Brownian trajectories. *Nat. Commun.* **9**, 1–9 (2018).
 33. Maragò, O. M., Jones, P. H., Gucciardi, P. G., Volpe, G. & Ferrari, A. C. Optical trapping and manipulation of nanostructures. *Nat. Nanotechnol.* **8**, 807–819 (2013).
 34. Pesce, G., Jones, P. H., Maragò, O. M. & Volpe, G. *Optical tweezers: theory and practice. European Physical Journal Plus* vol. 135 (Springer Berlin Heidelberg, 2020).
 35. Maragò, O. M. *et al.* Femtonewton force sensing with optically trapped nanotubes. *Nano Lett.* **8**, 3211–3216 (2008).
 36. Lechelon, M. *et al.* Experimental evidence for long-distance electrodynamic intermolecular forces. *Sci. Adv.* **8**, (2022).
 37. Seol, Y., Carpenter, A. E. & Perkins, T. T. Gold nanoparticles: enhanced optical trapping and. *Opt. Lett.* **31**, 2429–2431 (2006).
 38. Sbalzarini, I. F. & Koumoutsakos, P. Feature point tracking and trajectory analysis for video imaging in cell biology. *J. Struct. Biol.* **151**, 182–195 (2005).
 39. Huang, B., Wang, W., Bates, M. & Zhuang, X. Three-Dimensional Super-Resolution Reconstruction Microscopy. *Science (80-.)*. **319**, 810–813 (2008).
 40. Haro-González, P. *et al.* Optical trapping of NaYF₄:Er³⁺, Yb³⁺ upconverting fluorescent nanoparticles. *Nanoscale* **5**, 12192–12199 (2013).
 41. Wang, Y. *et al.* Nd³⁺-Sensitized Upconversion Nanophosphors: Efficient In Vivo Bioimaging Probes with Minimized Heating Effect. *ACS Nano* 7200–7206 (2013).
 42. Reece, P. J. *et al.* Characterization of semiconductor nanowires using optical tweezers. *Nano Lett.* **11**, 2375–2381 (2011).
 43. Thompson, R. E., Larson, D. R. & Webb, W. W. Precise nanometer localization analysis for individual fluorescent probes. *Biophys. J.* **82**, 2775–2783 (2002).
 44. Lelek, M. *et al.* Single-molecule localization microscopy. *Nat. Rev. Methods Prim.* **1**, 39 (2021).
 45. Sigal, Y. M., Zhou, R. & Zhuang, X. Visualizing and discovering cellular structures with super-resolution microscopy. *Science (80-.)*. **361**, 880–887 (2018).
 46. Liebel, M. *et al.* 3D tracking of extracellular vesicles by holographic fluorescence imaging. *Sci. Adv.* **6**, 1–9 (2020).
 47. Ouyang, W., Aristov, A., Lelek, M., Hao, X. & Zimmer, C. Deep learning massively accelerates super-resolution localization microscopy. *Nat. Biotechnol.* **36**, 460–468 (2018).
 48. Engelhardt, J. *et al.* Molecular orientation affects localization accuracy in superresolution far-field fluorescence microscopy. *Nano Lett.* **11**, 209–213 (2011).
 49. Rodríguez-Sevilla, P. *et al.* Optical Forces at the Nanoscale: Size and Electrostatic Effects. *Nano Lett.* **18**, 602–609 (2018).
 50. Loeb, A. L., Wiersema, P. H. & Overbeek, J. T. G. *The electrical double layer around a spherical colloid particle.* (MIT Press, 1961).
 51. Hunter, R. J. *Zeta Potential in Colloid Science: Principles and Applications.* (Academic Press, 1981).
 52. Nehme, E. *et al.* DeepSTORM3D: dense 3D localization microscopy and PSF design by deep learning. *Nat. Methods* **17**, 734–740 (2020).
 53. Friedrich, L. & Rohrbach, A. Surface imaging beyond the diffraction limit with optically trapped spheres. *Nat. Nanotechnol.* **10**, 1064–1069 (2015).
 54. Rodríguez-Sevilla, P. *et al.* Thermal Scanning at the Cellular Level by an Optically Trapped Upconverting Fluorescent Particle. *Adv. Mater.* **28**, 2421–2426 (2016).
 55. Pant, A., Xia, X., Davis, E. J. & Pauzauskie, P. J. Solid-state laser refrigeration of a composite semiconductor Yb:YLiF₄ optomechanical resonator. *Nat. Commun.* **11**, 1–7 (2020).
 56. Rodríguez-Sevilla, P., Arita, Y., Liu, X., Jaque, D. & Dholakia, K. The Temperature of an Optically

Data availability

The data that support the findings of this study are available within the paper and the Supplementary Information. Other relevant data are available from the corresponding author upon reasonable request.

Code availability

All custom code is available from the corresponding author upon reasonable request.

Acknowledgements

The authors thank Chennupati Jagadish for the equipment support and Mahnaz Maddahfar for polymer modification of Ln-NPs. The authors acknowledge financial support from the fellowship of China Postdoctoral Science Foundation (2022TQ0020), the International Postdoctoral Exchange Fellowship Program (YJ20220037). L.D. acknowledges the financial support from China Council scholarship (201809370076). This work was supported by a grant from the National Natural Science Foundation of China (General Program 62275010).

Author contributions

F.W. conceived and supervised the project. L.D., X.S., and F.W. constructed the optical setup. F.W. and S.S.J.W. built the theoretical simulation and analytical model. X.S. and P.N. built the deep learning model. S.W. synthesized the nanoparticles. L.D., H.Z., and X.Z. built the analysis of net charge of nanoparticles. L.D. and X.S. performed all the experiments. L.D., X.S. and F.W. analysed the results, prepared the figures, and wrote the manuscript in consultation with all authors.

Competing interests

The authors declare no competing interests.

Supplementary Files

This is a list of supplementary files associated with this preprint. Click to download.

- [SupplementaryInformation.docx](#)